

# Differently patterned airflows induced by 1-kHz femtosecond laser filaments in a cloud chamber

Haiyi Sun<sup>1</sup> · Hong Liang<sup>1</sup> · Yonghong Liu<sup>1</sup> · Jingjing Ju<sup>1</sup> · Yingxia Wei<sup>1</sup> · Cheng Wang<sup>1</sup> · Tiejun Wang<sup>1</sup> · Jiansheng Liu<sup>1</sup> · See Leang Chin<sup>2</sup> · Ruxin Li<sup>1</sup> · Zhizhan Xu<sup>1</sup>

Received: 20 April 2015 / Accepted: 28 August 2015 / Published online: 23 September 2015  
© Springer-Verlag Berlin Heidelberg 2015

**Abstract** Airflow induced by femtosecond laser (800 nm/1 kHz/25 fs) filamentation with different lengths was investigated in a laboratory cloud chamber. Various filament lengths were generated by adjusting laser energy and lens focal length. It was found that airflow patterns are closely related to filament intensity and length. Intense and long filaments are beneficial in updraft generation with large vortices above the filament, while intense and short filaments tend to promote the formation of well-contacted vortices below the filament. Differently patterned airflows induced elliptical snow piles with different masses. We simulated airflow in a cloud chamber numerically taking laser filaments as heat sources. The mechanisms of differently patterned airflow and snow formation induced by filaments were discussed.

## 1 Introduction

The self-focusing dynamics of femtosecond laser pulses is an active research area in nonlinear optics. Self-guided filaments are known to be generated by femtosecond laser pulses through a dynamic balance between the focusing Kerr nonlinearity and the defocusing effect of plasma

formation [1–5]. Filaments can propagate in air for distances from centimeters to meters with a nearly constant diameter. Also, it has been shown that clouds do not significantly affect the filamentation process, and they only dissipate quasi-linearly the energy in the beam envelope and diminish the number of filaments in proportion [6, 7]. Therefore, filaments are ideally suitable for atmosphere applications, including LIDAR (light detection and ranging) [8], remote sensing [9, 10], and lightning control [11]. In recent years, femtosecond laser-assisted water condensation has attracted considerable research attention and has been investigated in both cloud chambers and the atmosphere [12–19]. This is unlike the traditional method of spraying silver salt particles as seeds into clouds and thus provides a new tool for remote control of the nucleation processes in clouds.

Chemical and biological molecules/agents in air are likely to photoionization when a self-guided filament propagates in air because the intensity clamped in the filament core can reach an order of  $\sim 10^{14}$  W/cm<sup>2</sup> [2, 20]. The experimental measurements in cloud chambers demonstrated that femtosecond laser filaments could generate up to  $10^{14}$ ,  $3 \times 10^{12}$ , and  $3 \times 10^{13}$  molecules of O<sub>3</sub>, NO, and NO<sub>2</sub>, respectively [12]. Subsequently, HNO<sub>3</sub> with concentrations in the parts per million range would be produced by efficient oxidation reactions of nitrogen and would form binary compounds with water to serve as cloud condensation nuclei (CCN) [12, 14, 17]. In experiments on laser-assisted aerosol formation, it was also found that the presence of a few ppb of trace gases such as SO<sub>2</sub> and  $\alpha$ -pinene could clearly enhance the particle yield numerically, with the latter also enhancing the yield by mass under realistic atmospheric conditions [21]. Of course, similar compounds also exist in experimental cloud chambers, and thus, these compounds or their by-products would also be a part of CCN.

✉ Jiansheng Liu  
michaeljs\_liu@siom.ac.cn

✉ Ruxin Li  
ruxinli@mail.shcnc.ac.cn

<sup>1</sup> State Key Lab of High Laser Field Physics, Shanghai Institute of Optics and Fine Mechanics, Chinese Academy of Science, No. 390, Qinghe Road, Jiading District, Shanghai 201800, China

<sup>2</sup> Center for Optics, Photonics and Laser, Laval University, Quebec City, QC G1V 0A6, Canada

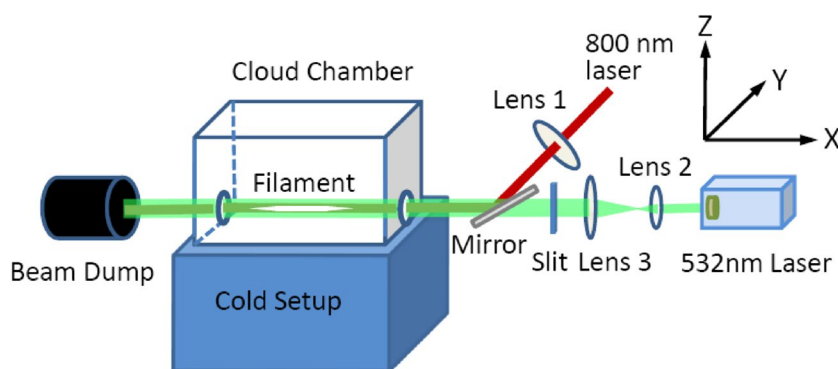


**Fig. 1** Schematic of the experimental setup. The femtosecond laser beam (red line) was focused by Lens 1 ( $f = 50$  or  $30$  cm), then passed through an entrance window ( $25 \times 25$  mm, 1.2-mm-thick fused silica), and exited at the opposite side through an exit window ( $25 \times 25$  mm, 1.2-mm-thick fused silica) into a beam dump. The

CCN need to grow to larger sizes of  $\sim 2$  mm in diameter for precipitation of condensed particles [19, 22], which is particularly important for practical applications. In 2012, our group conducted femtosecond laser-induced water condensation experiments by firing a 1-kHz/9 mJ/50 fs/800-nm laser into the super-saturated zone (relative humidity (RH)  $\sim 127$  %, temperature ( $T$ )  $\sim -29$  °C) of a laboratory diffusion cloud chamber ( $0.5 \times 0.5 \times 0.2$  m<sup>3</sup>) [17, 23]. Snow formation was observed just below the filament center for the first time. Meanwhile, an intense updraft with cyclone-like large vortices above the filament was produced, and a concave mirror with 70-cm focal length (1 kHz/50 fs) was used and generated laser filaments with lengths of 10 cm [17, 23]. We proposed that this continuous and intense updraft of warm, moist air plays an important role in the snow formation process via its interaction with the cold air above. In our later experiments, 1-kHz/2 mJ/45 fs/800-nm laser pulses were fired into a sub-saturated zone (RH  $\sim 73$  %,  $T \sim 4.3$  °C) in a laboratory diffusion cloud chamber ( $0.25 \times 0.18 \times 0.15$  m<sup>3</sup>), where a shorter filament with length of 1.0 cm was generated using a lens with focal length of 20 cm. Snow formation below the filament center was also observed, but differently patterned airflow was found [19, 24]. Scattering videos recorded from the side of the chamber show that the filament induced two vortices just below the filament, instead of the intense updraft with large vortices that had been observed previously.

This work aims to systematically study laser filament-induced differently patterned airflow and their dependence on the filament length and intensity, i.e., two regimes of vortices generation above and below the filaments, respectively. The experiments were performed in a laboratory cloud chamber ( $0.5 \times 0.5 \times 0.2$  m<sup>3</sup>) under illumination by the femtosecond laser pulses (800 nm, 25 fs) with a repetition rate of 1 kHz. Filaments with different lengths and

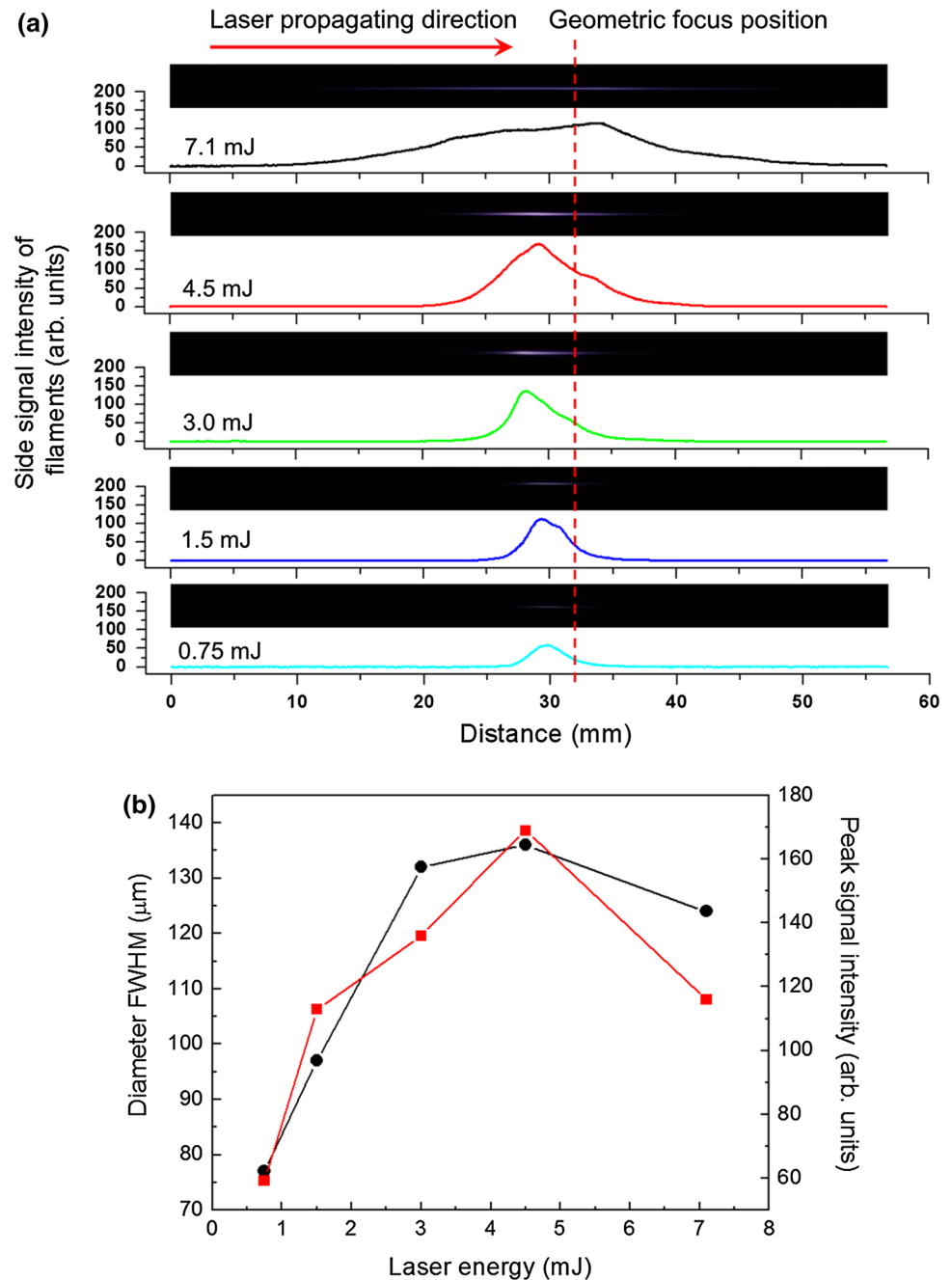
probe laser beam (green line) after being expanded in diameter by Lens 2 ( $f = 50$  cm) and Lens 3 ( $f = 10$  cm) and truncated by a slit was used for in situ light scattering measurements. The camera was positioned at the side of the cloud chamber ( $X$ - $Z$  section,  $+Y$  direction)

intensity were generated by adjusting the incident laser energy when the lens focal length was fixed at either 50 or 30 cm. Two-dimensional numerical simulations of the airflow were also carried out by assuming that the laser filaments act as a heat source. The simulations roughly agree with the experiments. The mechanisms of differently patterned airflow and snow formation induced by filaments with different lengths and intensity were discussed.

## 2 Experimental setup

A schematic of the experimental setup is shown in Fig. 1. A regenerative amplified Ti:sapphire laser centered at a wavelength of 800 nm that delivers 25-fs, 10-mJ, 1-kHz mode-locked pulses was used in our experiments. The laser pulses were focused by Lens 1. Lens 2 ( $f = 10$  cm) and Lens 3 ( $f = 50$  cm) were placed to act as a beam-expanding system for the probe beam. The maximum laser energy before the incident window of the cloud chamber was 7.1 mJ, and other laser energies such as 4.5, 3, 1.5, and 0.75 mJ were obtained by adjusting the electric current of the pump laser. To probe the airflow, a continuous wave (CW) 532-nm laser beam with 2.5-W output power was used after being expanded in diameter and truncated by a 30 mm (height)  $\times$  6 mm (width) slit. The side Mie scattering pattern of the airflow was recorded using a digital camera (Nikon D7000, Nikon Corporation, Japan). The cloud chamber size was 0.5 (length)  $\times$  0.5 (width)  $\times$  0.2 (height) m<sup>3</sup>, and a vertical temperature gradient was maintained in the chamber by using a refrigerating machine to cool the bottom base plate to a temperature of  $-46$  °C. During the experiments, the five faces other than the cold bottom plate were covered with 2-cm-thick insulation materials. A reservoir that was filled with distilled water was mounted at

**Fig. 2 a** Captured images (on top of each curve) and corresponding signal intensity of the laser filaments for different laser energy levels when the lens with 50-cm focal length was used. The images of filaments were captured by the Nikon D7000 camera ( $F = 5.6$ ,  $ISO = 800$ ,  $S = 1/10$  s). The arbitrary unit is the same for all curves across the figures. **b** FWHM diameter of the filament column (black circles, left scale) and the peak signal intensity (red squares, right scale) as a function of laser energy for the lens with 50-cm focal length



a height of 17 cm above the cold bottom plate inside the chamber. The quantity of water vapor inside the chamber was controlled by adjusting the electric current through a heating wire that was submerged in the water, and this current was set at  $\sim 1$  A in our experiments. We measured the increase in water temperature in a duration of experiment that is  $3.2$  °C. The laser filament height relative to the cold bottom plate of the cloud chamber was set at 10 mm, where the RH reached the maximum value of  $\sim 91$  % at  $\sim -13$  °C, based on measurements taken using a hygrometer (HMP110-C15-GZ, Vaisala, Finland).

### 3 Filamentation with 50-cm focal length lens

To obtain longer laser filaments, a lens with focal length of 50 cm was used. Figure 2a, b indicates the captured images and the corresponding signal intensities of the laser filaments in air, respectively. The filaments were captured by the Nikon D7000 digital camera ( $f$  number ( $F$ ) = 5.6, light sensitivity ( $ISO$ ) = 800, shutter speed ( $S$ ) =  $1/10$  s), and their intensities were transversely integrated. The filament is known to form through the dynamic balance between the Kerr focusing and multiphoton/tunnel

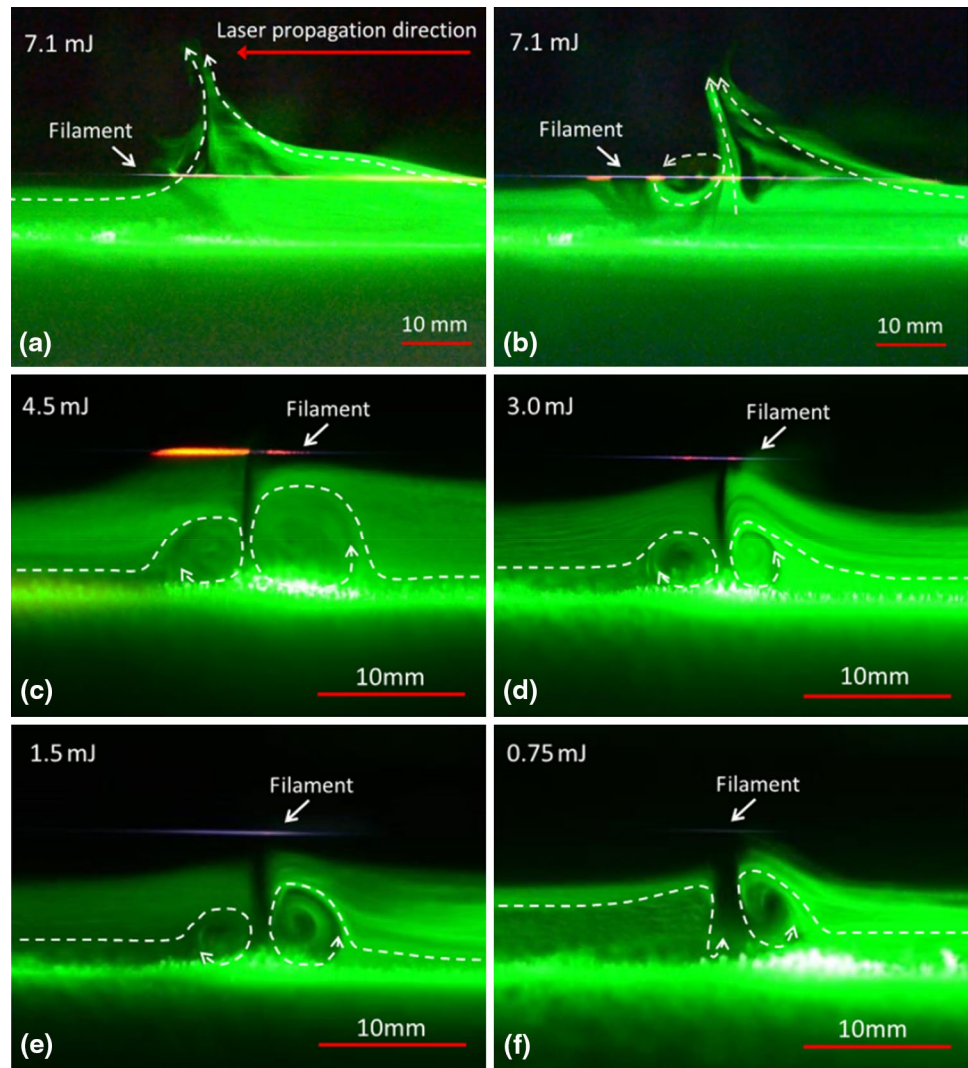
ionization (MPI)-induced plasma defocusing [1–5]. The plasma generation balances the self-focusing effect and leads to a clamped intensity. This in turn creates a long plasma channel in the air and results in fluorescent emission. The strength of the  $N_2^+$  fluorescence signal obtained at 391 nm by a spectrograph is proportional to the plasma density and can be used to measure the plasma density inside the filament [25–28]. Because a different detection method (Nikon camera) was used in our experiments, quantitative results for the peak plasma density inside the filament could not be given from Fig. 2a, b, but a qualitative result could be indicated. As shown in Fig. 2b, the peak signal intensity of the filament column rises slightly with increasing input laser energy from 0.75 to 4.5 mJ before an abrupt fall at the maximum laser energy of 7.1 mJ. It is implied that the change in the plasma density and the laser intensity inside the filament followed the same trend. The filament column length increases with increasing incident energy and had approximate values of 0.8, 1.6, 2.0, 3.0, and 5.0 cm as the laser energy increased from 0.75 to 7.1 mJ. We analyzed the gray distribution of imaged laser filaments (Fig. 2a) along the direction perpendicular to the laser filament axis. The full width at half maximum (FWHM) of filaments would be obtained by means of Gaussian fitting of the gray distribution curves. FWHM diameter at the position of the peak intensity initially rises from  $\sim 77$  to  $\sim 136$   $\mu\text{m}$  in the incident energy range from 0.75 to 4.5 mJ, and then decreases to  $\sim 124$   $\mu\text{m}$  when the energy reaches 7.1 mJ. It has been reported that because of the counterbalance between the input laser energy confined by external focusing and the defocusing effect of the plasma, the high-intensity core of the laser filament would be enlarged with increasing incident energy until multiple filaments appear [27, 28]. Based on this behavior, we estimate that the laser filament is probably a single filament in the energy range from 0.75 to 4.5 mJ, but the multiple filaments form at the energy of 7.1 mJ and thus lead to the abrupt falls in the peak signal intensity and the FWHM diameter. This is also confirmed by our observations (of at least two filaments) on a paper screen positioned far away from the exit window of the laser beam.

In Fig. 3, the side Mie scattering patterns of the airflow (video frame figure) induced by the laser filaments are shown as the incident energy was adjusted for the lens with 50-cm focal length. The Mie scattering is from the laser-generated particles. Larger particles would generate stronger side Mie scattering. In the case of the energy of 7.1 mJ, an updraft is generated above the filament because of the heating effect of the laser filaments. Sometimes, we observed one small vortex near the filament, as shown in Fig. 3b. A thick mist or irregular airflow forms below the long filament. In our previous experiments, where a concave mirror with 70-cm focal length (1 kHz/50 fs, 8.5 mJ)

was used to generate laser filaments with lengths of 10 cm, similarly patterned but more intense updrafts with large vortices above the filament were induced [17]. Intense updrafts with vortices above the filament were not often observed here, probably because the present filament is not strong enough (lower plasma density) as a result of the formation of multiple filaments, although a longer filament of  $\sim 5$  cm was used. As the incident energies were gradually reduced to 4.5, 3.0, 1.5, and 0.75 mJ, two small vortices appeared directly below the filaments (Fig. 3c–f). The same vortices also appeared when a weaker laser energy (2 mJ) was used with a shorter filament length (1.1 cm) in our previous experiments [19]. The airflow patterns here induced by the filaments with different lengths confirm the previous experimental observations [17, 19, 23]. The airflow is mainly generated by the temperature gradient between the laser filament and atmosphere around. The heat release by the laser filament is through plasma recombination and relaxation processes [29]; therefore, a higher plasma density would induce greater heat release and a larger temperature gradient between the laser filament and atmosphere around. A longer filament would generate greater heat release than that by a shorter filament at the same filament intensity. Consequently, intense and long filaments are beneficial for generation of the intense airflow. In the present work, because the heat released from the filament at the maximum energy of 7.1 mJ is still insufficient, only an updraft with a low airflow velocity above the filament was observed. An intense updraft with large vortices above the filament would be produced as observed in our previous experiments with increasing intensity and length of laser filament [17]. The formation of vortices below the filament center is mainly dependent on the thermal gradient associated with each end of the filaments, which will be analyzed in the following numerical simulation section.

A pile of snow that was located just below the filament center was induced after 1 h of laser irradiation, as shown in Fig. 4. 1-h-long laser irradiation is not necessary for producing the snow piles. In the experiments, a pile of snow appeared after  $\sim 20$ -min laser irradiation, and the masses of snow piles would increase as the laser irradiation duration increases. We extended the laser irradiation duration to 1 h just to make clear comparisons of the shapes and masses of snow piles induced by different laser filaments. The background (Fig. 4f) after 20 min of cooling before the laser was fired into the chamber was also given as a comparison. A thin layer of frost was seen to form on the bottom plate before firing of the laser. The circle at the plate center had less frost coverage, which was the result of a slightly higher temperature at the center caused by ring-shaped cooling pipes that were installed under the bottom plate. After 1 h of irradiation of the laser filament, snow piles with oval shapes were produced, except at the

**Fig. 3** Side Mie scattering patterns of the airflow (captured by video frames: 40 laser shots) induced by the filament for different laser energies (**a**, **b** 7.1 mJ, **c** 4.5 mJ, **d** 3.0 mJ, **e** 1.5 mJ, and **f** 0.75 mJ) with the focal length of the lens being fixed at 50 cm. The laser propagation directions in **b–f** were same as that in **a**. The *white dashed lines* in all images are artificially created guidelines to show the airflow directions

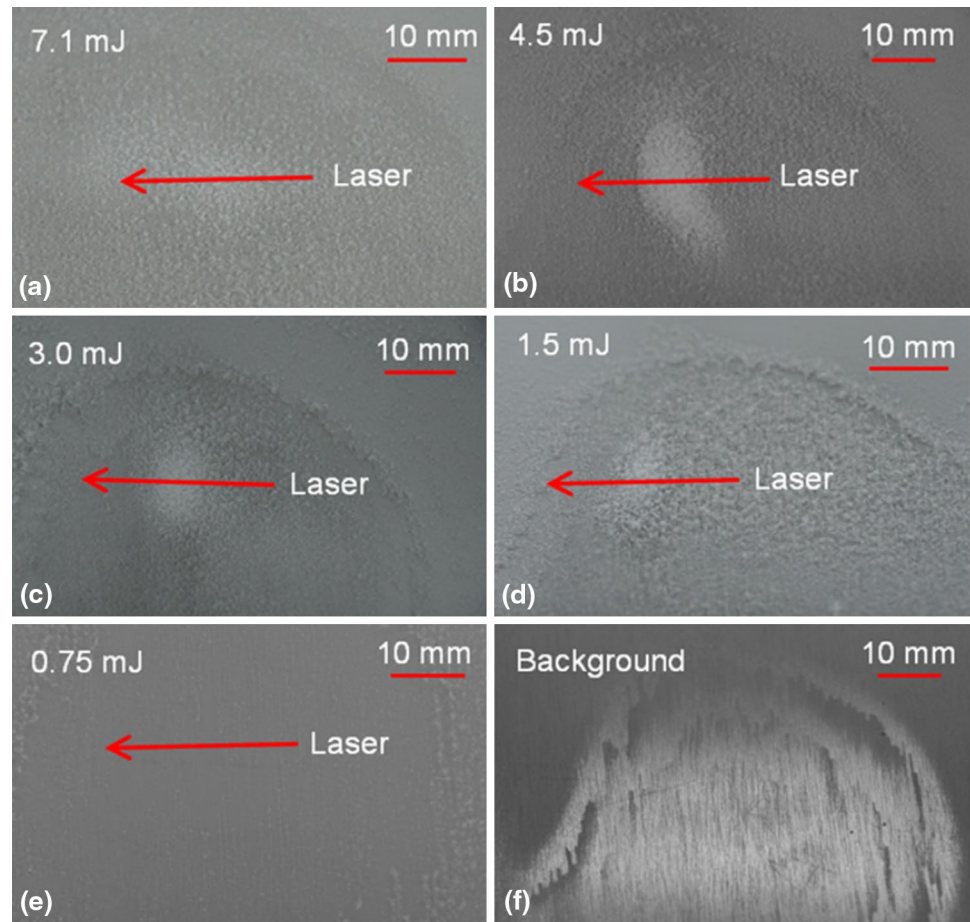


laser energy of 0.75 mJ. The amount of snow produced after 1 h of laser irradiation was weighed (Fig. 5a) and was found to increase with increasing laser energy in the range from 0.75 to 4.5 mJ before decreasing at the highest laser energy of 7.1 mJ. The heaviest snow pile for the laser energy of 4.5 mJ weighed about 18–27 mg/1 h, while hardly any snow formed below the filament for the laser energy of 0.75 mJ. The same method as that given in [17] was used to roughly estimate the maximum airflow velocity around the filaments. It was found that the airflow velocity changes in the same way as the mass of the snow pile in the same laser energy range, indicating that the mass of the snow pile is strongly dependent on the airflow velocity. Higher airflow velocities lead to larger amounts of laser-induced snow. The maximum airflow velocity was estimated to be 10.7–12.6 cm/s at the laser energy of 4.5 mJ (Fig. 5b). The maximum airflow velocity was located at the middle of the updraft or the vortices when different laser energies were used, which is similar to previous findings

[17–19]. However, the maximum updraft velocity for the laser energy of 7.1 mJ (3.0–6.0 cm/s) is much smaller than that induced by a 10-cm-long filament in our earliest work, where the experimental value is ~60 cm/s [17], indicating that the filament in the present experiments was weaker in intensity (i.e., lower in plasma density and level of heat release).

Results shown in Fig. 5a, b indicate that both the snow pile mass and the airflow velocity are closely related to the peak signal intensity of the laser filaments. Figure 5c shows the strong dependence of snow amount on airflow velocity. A higher peak signal intensity means higher laser intensity and higher plasma density inside the filament, which would induce greater heat release and result in airflow and formation of vortices with a faster velocity. We estimated the saturation ratio of the vapor relative to water inside the vortices above and below the laser filaments according to the method given in [19, 24], which is about 83 and 230 % for the vortices above and below the filaments, respectively.

**Fig. 4** Laser filament-induced snow piles under different laser energies (**a** 7.1 mJ, **b** 4.5 mJ, **c** 3.0 mJ, **d** 1.5 mJ, **e** 0.75 mJ, and **f** background before laser firing) with the focal length of the lens being fixed at 50 cm. *Red arrow lines* indicate the laser propagation direction. All the images are *top views*



Thus, the higher density condensation nuclei around the laser filament would be activated and would grow in size inside the vortices, where the humidity was sub-saturated or super-saturated. The higher airflow velocity would also increase the transport efficiency of water molecules carried by airflow involved the vortices or passing by the snow pile. Therefore, a larger amount of snow would be produced.

#### 4 Filamentation with 30-cm focal length lens

The same experiments were conducted using the lens with 30-cm focal length to compare the patterns of airflow and snow formation induced by the different filaments. Figure 6a, b show captured images of the laser filaments and the corresponding signal intensity distributions when the lens with 30-cm focal length was used. We observe an initial steep rise in both the signal intensity and the filament diameter while the laser energies increased from 0.75 to 3.0 mJ, before the slope changed toward constant values at the higher laser energies from 3.0 to 7.1 mJ. The steep rise in the side signal intensity at lower laser energies indicates a sharp increase in the plasma density inside the filament

[27, 28]. For the higher laser energies from 4.5 to 7.1 mJ, the peak signal intensity nearly saturates, which indicates saturation of the peak plasma density inside the filament volume. The diameter of the filament volume increases from  $\sim 133 \mu\text{m}$  to a nearly constant value of  $\sim 260 \mu\text{m}$  with increasing laser energies from 0.75 to 7.1 mJ. The saturation of the peak plasma density and the nearly constant value for the filament diameter at higher energies from 4.5 to 7.1 mJ show an energy limit for a single filament, after which the multiple filaments probably appear [28]. When compared to the lens with the 50-cm focal length, the filament for the lens with 30-cm focal length is shorter, but is stronger in side signal intensity and larger in diameter at the same laser energy. By using a shorter focal length lens, the laser energy can be confined to a smaller volume, resulting in higher laser intensity inside the filament when the laser pulses self-focus. Thus, to counterbalance the stronger pulse convergence, a higher plasma density would be generated, accompanied by a filament volume with a broader waist because plasma defocused more efficiently the pulse [27].

The stable vortices immediately below the filaments were observed for the laser energies from 0.75

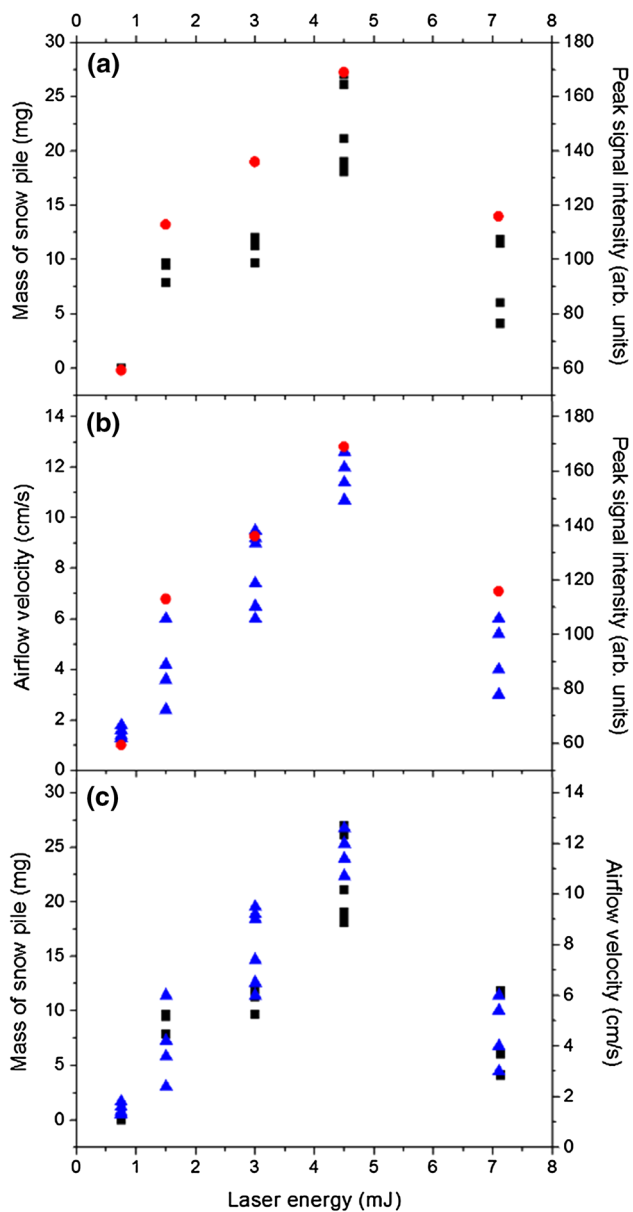
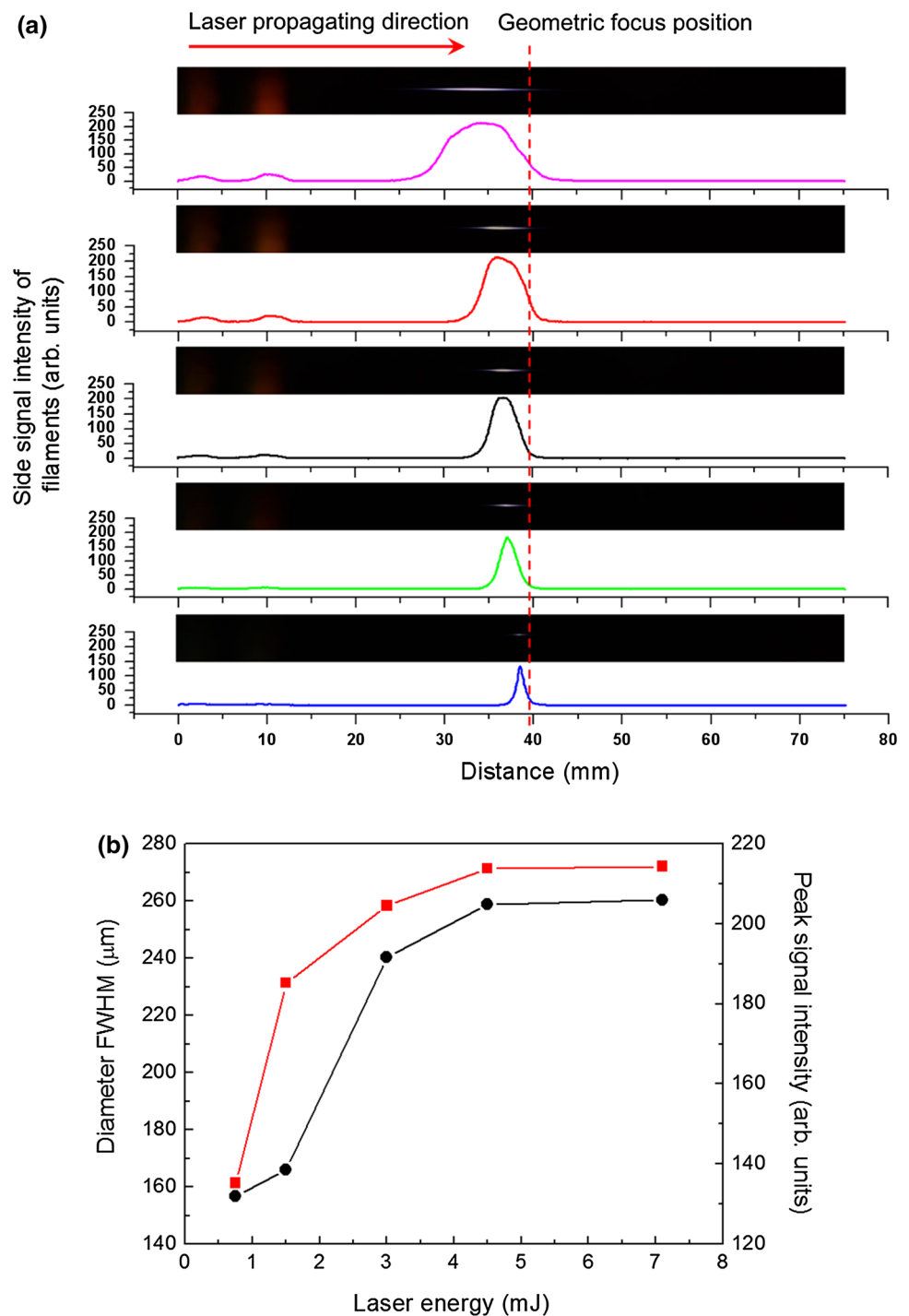


**Fig. 5** Links between the **a** mass of the snow pile below the laser filaments (black squares, left scale) and peak signal intensity of the filaments (red circles, right scale), **b** airflow velocity (blue triangles, left scale) and peak signal intensity of the filaments (red circles, right scale), and **c** mass of the snow pile below the laser filaments (black squares, left scale) and airflow velocity (blue triangles, right scale) under different laser energies with the lens focal length being fixed at 50 cm

to 7.1 mJ (Fig. 7a–e). In contrast, updrafts with vortices above the filament, as shown in Fig. 3a, were not observed, although stronger filaments were used here. By comparing the airflows formed with 4.5 and 3 mJ energies (Figs. 3, 7), it is found that there is red fluorescence emission along the filaments, which results from  $H_{\alpha}$  (656.27 nm) of laser filament interaction with water

droplets [30, 31]. We measured  $H_{\alpha}$  (656.27 nm) line in other experiments with the same experimental conditions using a grating spectrometer (Andor 303i). We also found that the gap separating the two vortices below the filaments corresponds to a partial extinction of red fluorescence emission along the filaments, while intense red fluorescence emission corresponds to the intense airflow below. This is also confirmed by other video frame figures and captured images (not shown here) for the cases of 4.5 and 3.0 mJ energies. Because the two vortices which are accompanied with small-size water droplets are induced on both sides below the filaments, a gap is formed between the two vortices where there will be few water droplets, and thus, very weak red fluorescence emission is observed. Figure 8 shows piles of snow that were produced just below the filament. These snow piles are also oval in shape. The mass of the snow pile (Fig. 9a) initially increases steeply in the laser energy range from 0.75 to 3.0 mJ and then changes slowly at higher energies from 3.0 to 7.1 mJ. It is noted that there is a small increase in the mass of the snow pile between two high energies of 7.1 and 4.5 mJ in spite of their comparable side signal values. This is resulted from the longer filament for 7.1 mJ energy (Fig. 6a), followed by a little more heat release that induces the heavier mass of snow pile. The maximum airflow velocity around the filament is shown in Fig. 9b, which initially rises rapidly as the laser energies increase from 0.75 to 3.0 mJ and then increases more slowly until a plateau region is reached in the laser energy range from 3.0 to 7.1 mJ. It is found that both the mass of snow piles and the airflow velocity are closely related to the intensity of laser filament. Additionally, the mass of snow piles also has the strong link with the airflow velocity, as indicated in Fig. 9c. These trends are similar to the results for the lens with 50-cm focal length. The snow pile masses are more than that induced by using the lens with 50-cm focal length under the same laser energy conditions. The lens with the shorter focal length has higher efficiency for snow formation because of the higher intensity inside the laser filament and stronger airflow motion. The peak signal intensity of the laser filament would vary with the focal lengths of the different lenses. Under the same laser energy conditions, longer focal lengths produce longer filament lengths but weaker filament intensities. This can be explained based on the balance between the external focusing and self-focusing [27]. A lens with a shorter focal length would confine the laser energy into a smaller volume, and thus, higher intensity would be generated inside the filament as the laser pulses self-focused [27]. Higher intensity inside the filament would induce the generation of more CCN and airflow with the higher velocity; therefore, the mass of snow pile would be heavier.

**Fig. 6** **a** Captured images (on top of each curve) and corresponding signal intensity of the laser filaments under different laser energies when the lens with 30-cm focal length was used. The shooting conditions of images of filaments were the same as that used in Fig. 2a. The arbitrary unit is the same for all curves across the figures. **b** FWHM diameter of the filament column (black circles, left scale) and the peak signal intensity (red squares, right scale) as a function of laser energy for the lens with 30-cm focal length



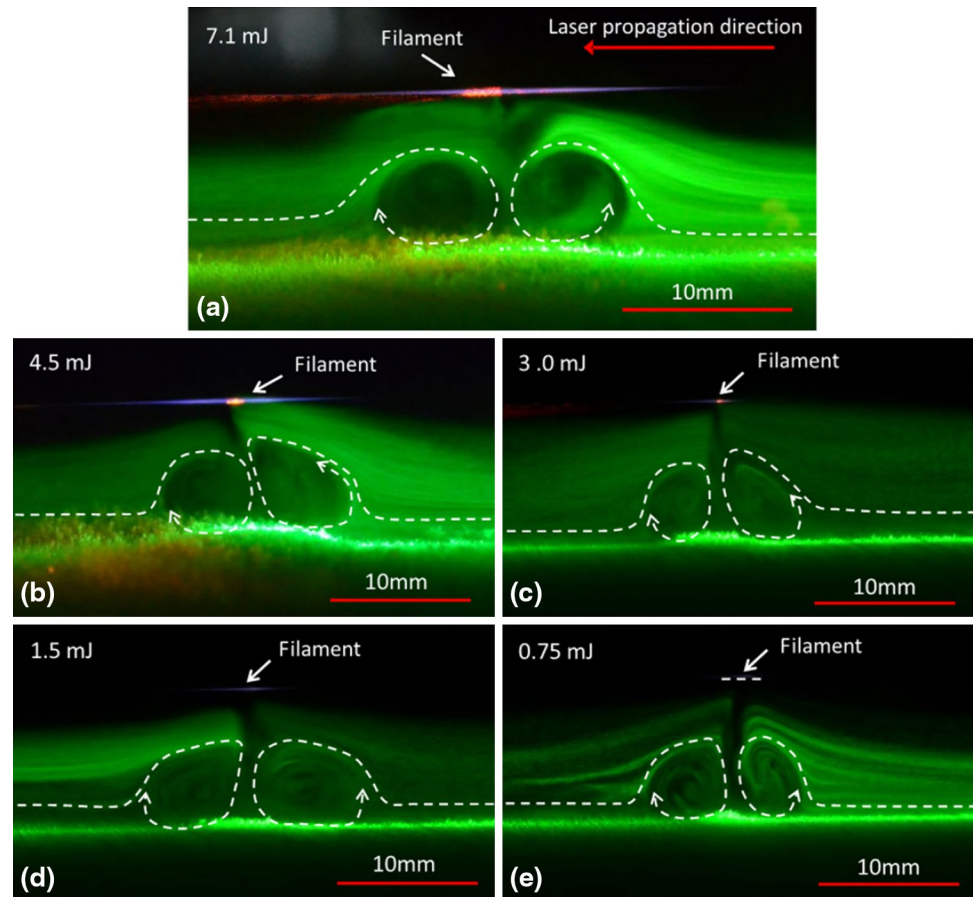
## 5 Numerical simulation and discussion

To gain an insight into the airflows induced by the different filaments, we simulated the flow fields in the cloud chamber numerically using a two-dimensional model (with  $X$ - $Z$  cross section containing the laser filament and perpendicular to the cold plate). In the model, some typical filaments

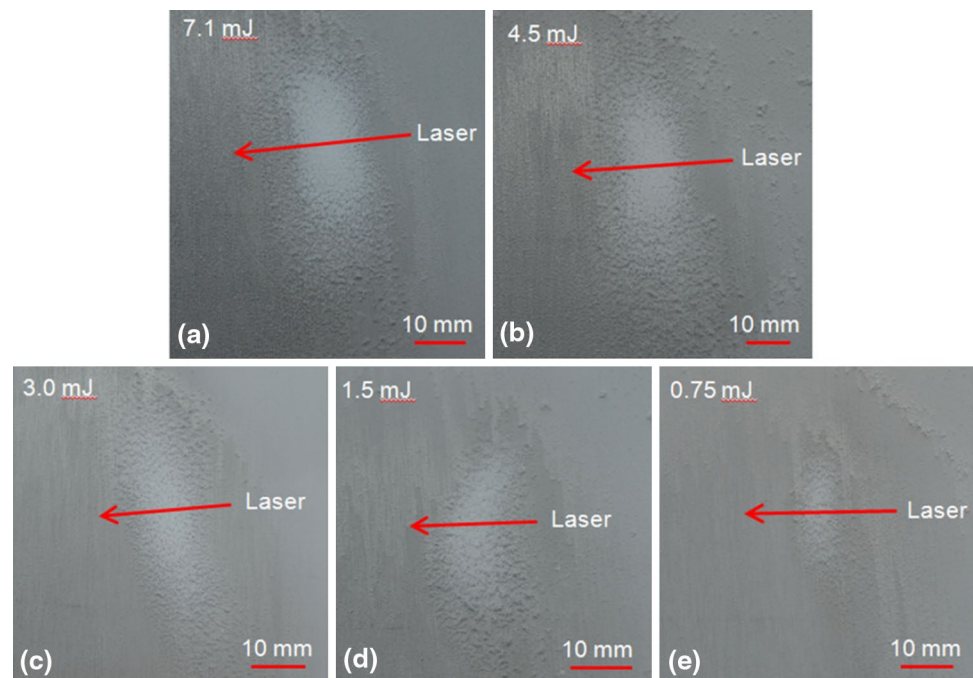
were chosen to compare the airflow patterns induced by filaments with different lengths. In the case of the  $f = 50$ -cm lens, a 5.0-cm-long filament with a diameter of 123  $\mu\text{m}$  for laser energy of 7.1 mJ, a 3.0-cm-long filament with a diameter of 135  $\mu\text{m}$  for laser energy of 4.5 mJ, and a 2.0-cm-long filament with a diameter of 127  $\mu\text{m}$  for laser energy of 3.0 mJ were chosen. For the  $f = 30$ -cm lens, a 0.3-cm-long filament with a diameter of 133  $\mu\text{m}$  for laser energy



**Fig. 7** (Color online) Video frame figure of airflow patterns (40 laser shots) induced by the laser filament under different incident energies (**a** 7.1 mJ, **b** 4.5 mJ, **c** 3.0 mJ, **d** 1.5 mJ, **e** 0.75 mJ) with the focal length of the lens being fixed at 30 cm. The laser propagation directions in **b–e** were same as that in **a**. The *white dashed lines* (except for the filament shown in **e**) in all images were intended as guidelines for the eyes for the airflow directions



**Fig. 8** Laser filament-induced snow pile under different incident energies (**a** 7.1 mJ, **b** 4.5 mJ, **c** 3.0 mJ, **d** 1.5 mJ, **e** 0.75 mJ) with the focal length of the lens being fixed at 30 cm. The *red arrow lines* indicate the direction of laser propagation. All the images are *top* views



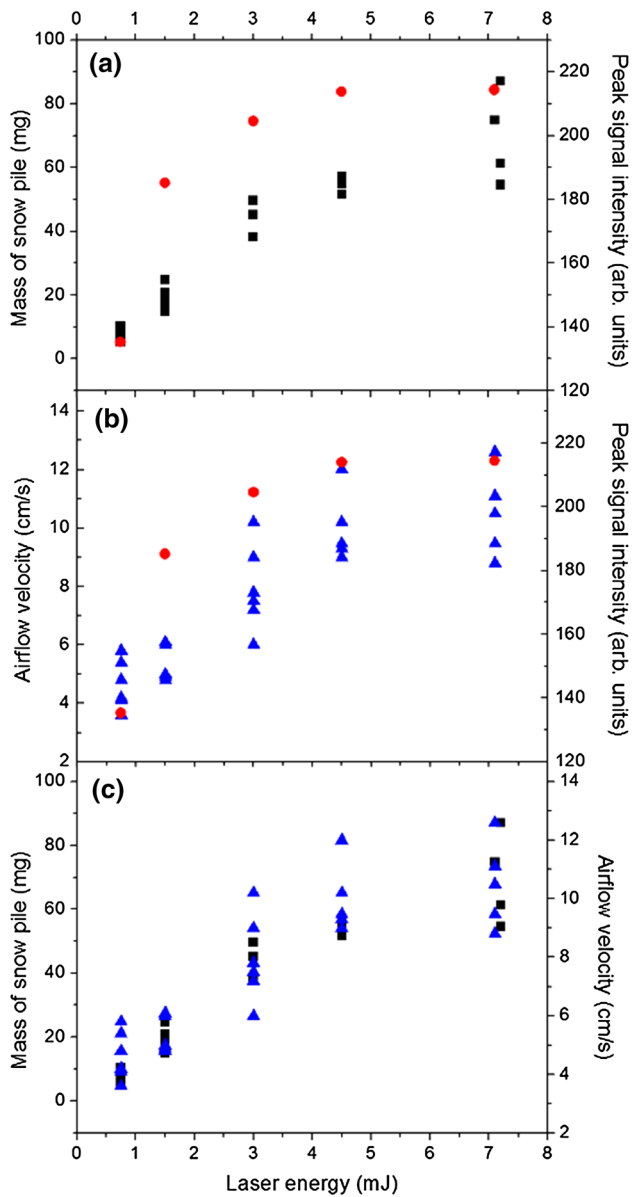


**Fig. 9** Links between the **a** mass of the snow pile below the laser filaments (black squares, left scale) and peak signal intensity of the filaments (red circles, right scale), **b** airflow velocity (blue triangles, left scale) and peak signal intensity of the filaments (red circles, right scale), and **c** mass of the snow pile below the laser filaments (black squares, left scale) and airflow velocity (blue triangles, right scale) under different laser energies with the lens focal length being fixed at 30 cm

of 0.75 mJ was chosen. There is no way to avoid plasma generation because the ultrashort characteristic of fs pulses makes the intensity of laser filaments reach  $10^{13}$ – $10^{14}$  W/cm<sup>2</sup>. The generated plasma that contains different kinds of energetic particles will expand toward the background gas driven by the energy locally deposited on the target by the laser pulses [32–34]. The formation of an outward-propagating pressure wave, that is, shock wave, leaves in the

volume initially occupied by the filament a lower-density channel [35]. Lots of measurement data have been reported about the decay time of plasma expansion and shock wave. A typical timescale is ns to tens of ms [34–36]. However, it is worth noting that the outward-propagating shock wave makes it present the propagation geometry with a cylindrical symmetry along the filament axis, rather than the symmetry along the center line perpendicular to the filament axis [37], which is different from the airflow patterns observed in our experiments. Therefore, we thought the effect of plasma expansion and shock wave probably did not play a dominant role in the process of airflow motion. In addition, heat effect is expected to be dominant since a temperature gradient is also imposed in the present setup. Therefore, the coupled mass–heat transfer and flow processes, including the continuity, energy, and the Reynolds-averaged Navier–Stokes (RANS) momentum equations of the gas, were mathematically solved in the model. All equations are written assuming steady-state and thermodynamic equilibrium.

The continuity equation is described by the equation [38–40]

$$\frac{\partial(\rho u)}{\partial x} + \frac{\partial(\rho v)}{\partial z} = 0 \quad (1)$$

where  $u$  and  $v$  are the airflow velocities at  $x$  and  $z$  direction, respectively.  $\rho$  is the density of air.

Accounting for the heat transport due to conduction and air transport, the energy equations are given by [39–41]

$$\nabla \cdot (\rho \vec{u} h) = -\nabla \cdot q \quad (2)$$

$$\nabla \cdot (\rho \vec{v} h) = -\nabla \cdot q \quad (3)$$

$$-\nabla \cdot q = \nabla \cdot (\lambda \nabla T) + S \quad (4)$$

$$h = c_p T, \quad (5)$$

where  $h$  is the specific enthalpy,  $q$  is the heat flux, and  $c_p$  is the specific heat capacity.  $T$  is the temperature, and  $S$  is the internal heat source.  $\lambda = \rho \alpha c_p$  is the thermal conductivity, and  $\alpha$  is the thermal diffusivity. As boundary conditions, setting the temperatures  $T_0$  at the bottom of the chamber as  $-46$  °C, and  $T_L$  at the top of the chamber as the room temperature, respectively, the corresponding specific enthalpy can be calculated. Two side walls were assumed to be adiabatic. In this model, the laser filament zone was treated as a heat flux source. We made a careful measurement of the energy deposited by the incident laser pulse into the filament. The laser power values before and just after the filaments were measured using the power meter (PM 30, Coherent Inc.) in the cloud chamber. Thus, the energy losses at different incident energies could be calculated. Each value of energy loss is mean of three measurements.

For the  $f = 50$ -cm lens, the energy deposited by the incident laser pulse into the filament is  $\sim 5\%$  for the 7.1 mJ, which is close to the measured value at the input energy of 0.75 mJ. Then, the deposited energy into the filament increases to  $\sim 6$  and  $8\%$  for 3.0 and 4.5 mJ, respectively. Higher filament energies were obtained in the focal region when the stronger focusing geometry (30 cm lens) was used. The energy deposited by the incident laser pulse into the filament rises to about  $18\%$  at the maximum input energy of 7.1 mJ and then decreases as the input energy decreases (30 cm lens). For the chosen filament that was generated by using the lens with 30-cm focal length and 0.75 mJ energy in our numerical simulation, the deposited energy into the filament is  $\sim 6\%$ , which is close to the value obtained for the 7.1 mJ case with the  $f = 50$ -cm lens. Based on these measurements, the calculated heat flux of the laser filament is  $\sim 1.8 \times 10^4$ ,  $2.8 \times 10^4$ , and  $2.3 \times 10^4$  W/m<sup>2</sup> for the 7.1, 4.5, and 3.0 mJ case with the  $f = 50$ -cm lens, respectively, and  $\sim 3.6 \times 10^4$  W/m<sup>2</sup> for 0.75 mJ energy with the  $f = 30$ -cm lens. Air was assumed as an ideal gas, and room-temperature values of specific heat and thermal diffusivity were used.

The RANS momentum equation is as follows [39–41]

$$\frac{\partial(\rho u)}{\partial t} + \nabla \cdot (\rho \vec{u} u) = \nabla \cdot (\mu \nabla u) - \frac{\partial p}{\partial x} - V_x \quad (6)$$

$$\frac{\partial(\rho v)}{\partial t} + \nabla \cdot (\rho \vec{u} v) = \nabla \cdot (\mu \nabla v) - \frac{\partial p}{\partial y} - V_z + \rho g. \quad (7)$$

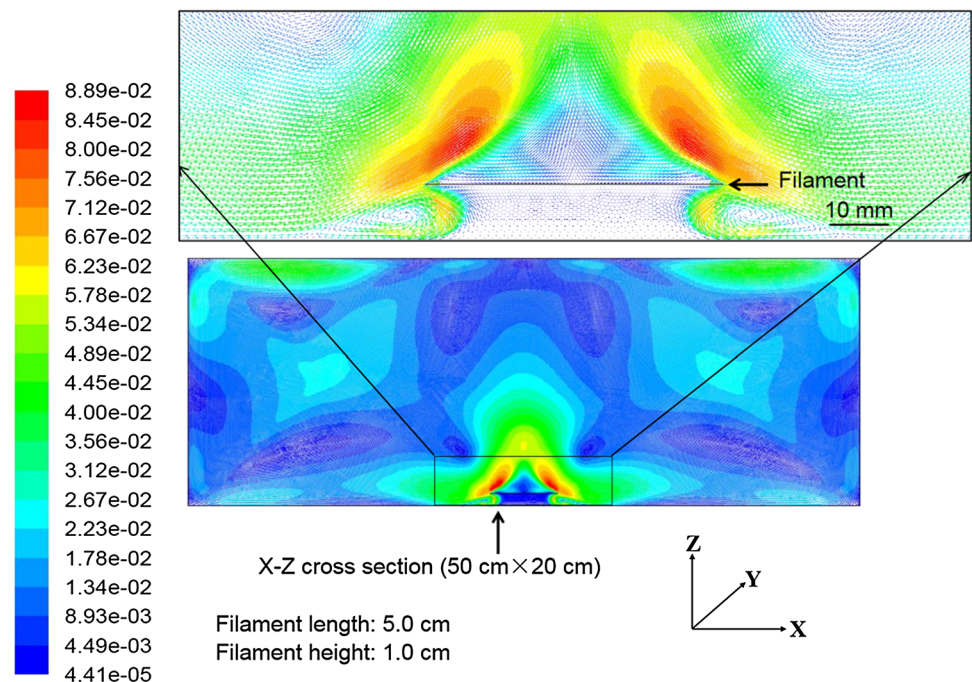
here  $\mu$  is the dynamic viscosity of air,  $p$  is the total pressure, and  $V_x$  and  $V_z$  are additional viscosity terms not included in

$\nabla \cdot (\mu \nabla u)$  and  $\nabla \cdot (\mu \nabla v)$ , which are individually solved by Reynolds stress models (RSM) [42].  $g$  is the gravitational acceleration.

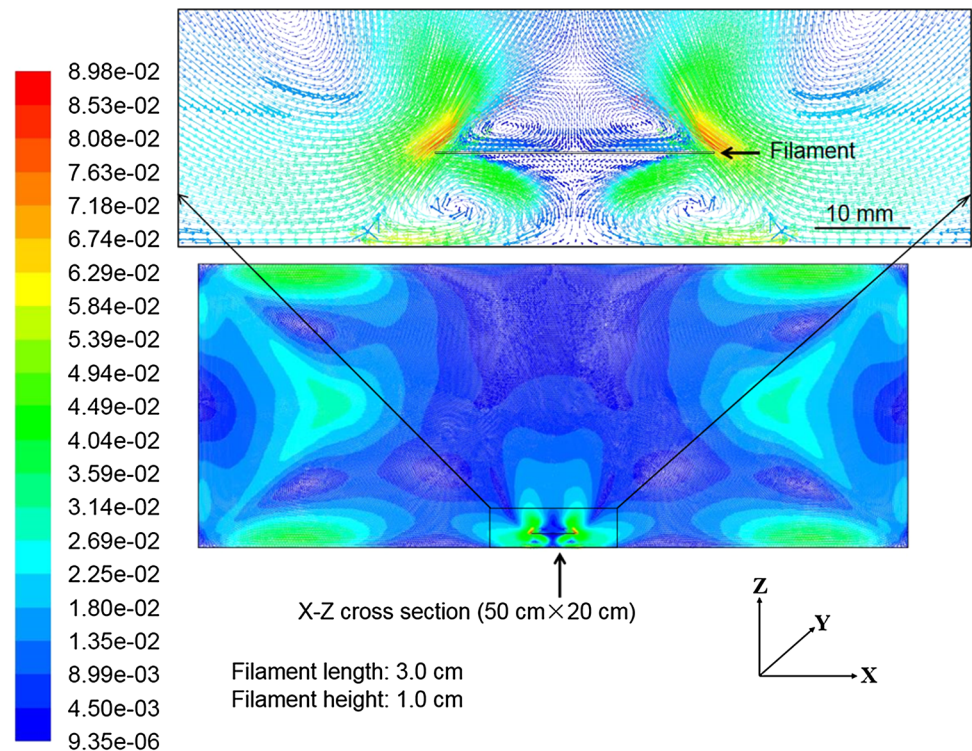
In this work, all equations were solved by a commercial program, Fluent 6.3, in which the control volume method was used to discretize the transport equations. The solutions to the density, momentum, energy, and Reynolds stress equations were approximated by the second-order up-wind differencing scheme to improve the precision of the calculation. The pressure–velocity coupling scheme was pressure implicit with splitting of operators (PISO) [18, 38]. As a convergence criterion, the monitored residuals of all variables were  $< 10^{-6}$ .

Figure 10 shows the 2D simulation results of the airflow for the energy of 7.1 mJ. We can clearly observe the updraft (the red and green areas above the filament in Fig. 10), which flows from the two sides of the filament to the middle area. The weak airflow (the blue area in Fig. 10) appears between the left and right updrafts. The airflow pattern and maximum airflow velocity position agree well with the experimental results shown in Fig. 3a. In the simulation results, we also found that two vortices appeared at the two sides of the filament, but they do not touch each other because a longer filament is used. This phenomenon was hardly observed in the experiments probably because of the irregular changes in multiple filaments [43, 44]. The simulated airflow velocity (8.89 cm/s) is slightly larger than the experimental values (3.0–6.0 cm/s) because a filament with a uniform intensity distribution was considered in the model.

**Fig. 10** Two-dimensional simulation results of airflow in an  $X$ – $Z$  cross section (the bottom  $X$ – $Y$  section ( $Z = 0$ ) was the cold plate) containing 5.0-cm-long laser filament for an energy of 7.1 mJ with a 1-cm filament height to the cold plate using the lens with 50-cm focal length. The velocity vectors are colored based on their velocity magnitude (m/s)



**Fig. 11** Two-dimensional simulation results for airflow in the  $X$ - $Z$  cross section (the bottom  $X$ - $Y$  section ( $Z = 0$ ) was the cold plate) containing 3.0-cm-long laser filament for an energy of 4.5 mJ with a 1-cm filament height to the cold plate using the lens with 50-cm focal length. The velocity vectors are colored based on their velocity magnitude (m/s)



As the filament length is shortened to 3 cm, the 2D simulated flow field is shown in Fig. 11. The gap between the two vortices below the filament also shortens, and the vortices contact each other at the boundary with the slower velocity (the blue area between the two vortices in Fig. 11). In the experiments (Fig. 3c), the airflow velocity is the fastest at the middle boundary between the two vortices and the slowest at the gap between the two vortices (black gap between two vortices in Fig. 3c). This agrees well with the simulated results (green boundary and blue area between the two vortices below the filament in Fig. 11). A larger gap appears between the two simulated vortices than between the experimental vortices, which probably resulted from the filament with length of <3 cm in the experiments because of the nonuniform intensity distribution in that filament. The simulated airflow velocity of 8.98 cm/s is close to the experimentally measured values (10.7–12.6 cm/s).

Figure 12 shows the 2D airflow simulation results where the length of the heating filament is 2 cm. The two vortices appear below the filaments and contact well at the boundary with the faster airflow velocity (green area between the two vortices below the filaments in Fig. 12). The patterns of the two simulated vortices are in accordance with the experimental observations (Fig. 3d). The simulated maximum airflow velocity is 9.26 cm/s, which is close to the experimental values of 6.0–9.3 cm/s.

When the filament length is reduced to 0.3 cm, the 2D simulated flow field is as indicated in Fig. 13. It is found that two well-contacted vortices below the filament appear

when an intense and shorter filament was used. This agrees well with the experimental observations shown in Fig. 7e. The simulated maximum airflow velocity is 5.74 cm/s, which falls within the range of the experimental measurements (3.6–5.8 cm/s).

It is found from the simulation results that the vortices below the laser filaments always appear. The formation of vortices below the filaments is probably due to the temperature gradient associated with each end of the filaments. This temperature gradient is related to the intensity profiles inferred from Figs. 2a and 6a. In order to simulate the effect of filaments, the laser filaments are set as a heat flux source with a certain length in our model. Therefore, an abrupt drop of heat release would appear at two ends of filaments, which would result in a temperature gradient between the end and inside of filament. This temperature gradient would further generate a pressure gradient, that is to say, the pressure at the end of filament is higher than that inside of filament due to the rising of hot air. Consequently, a part of air passing the end of filament would flow downward and generate the vortices. Because the typical length of vortex is about 10 mm based on the simulations, two vortices would contact with each other well when the length of filament is comparable to or less than double the length of vortex.

For the longest filament generated by the lens with 50-cm focal length at 7.1 mJ energy, the updraft and vortices above the filament were observed in both the experimental (Fig. 3a, b) and simulating results (Fig. 10). However, the

**Fig. 12** Two-dimensional simulation results for airflow in the  $X$ - $Z$  cross section (the bottom  $X$ - $Y$  section ( $Z = 0$ ) was the cold plate) containing 2.0-cm-long laser filament for an energy of 3.0 mJ with 1-cm filament height to the cold plate using the lens with 50-cm focal length. The velocity vectors are colored based on their velocity magnitude (m/s)

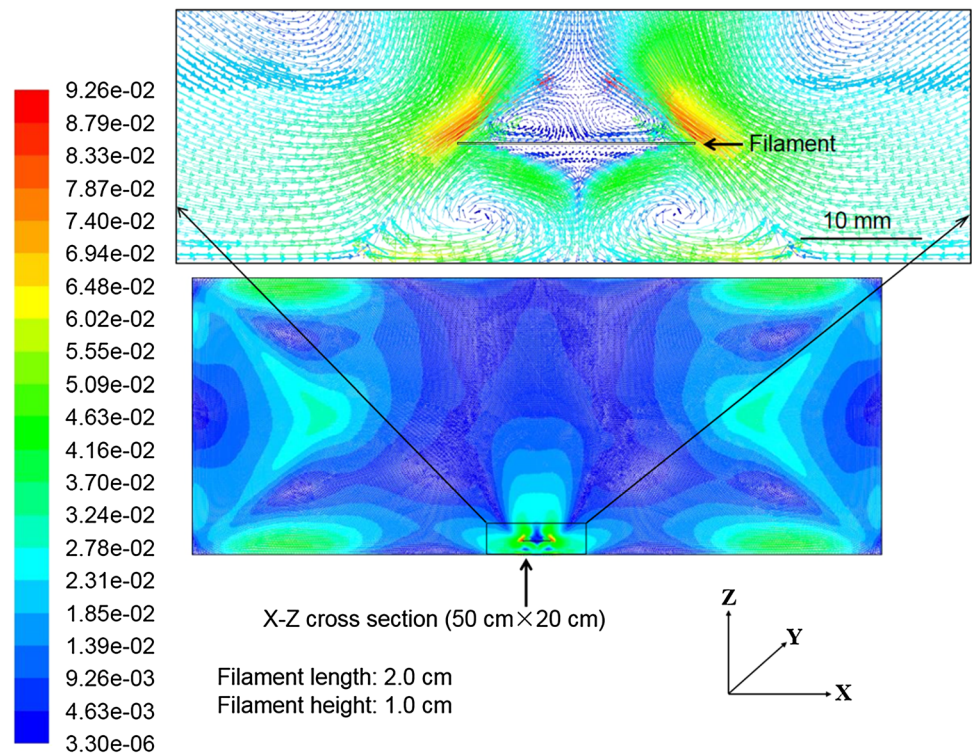
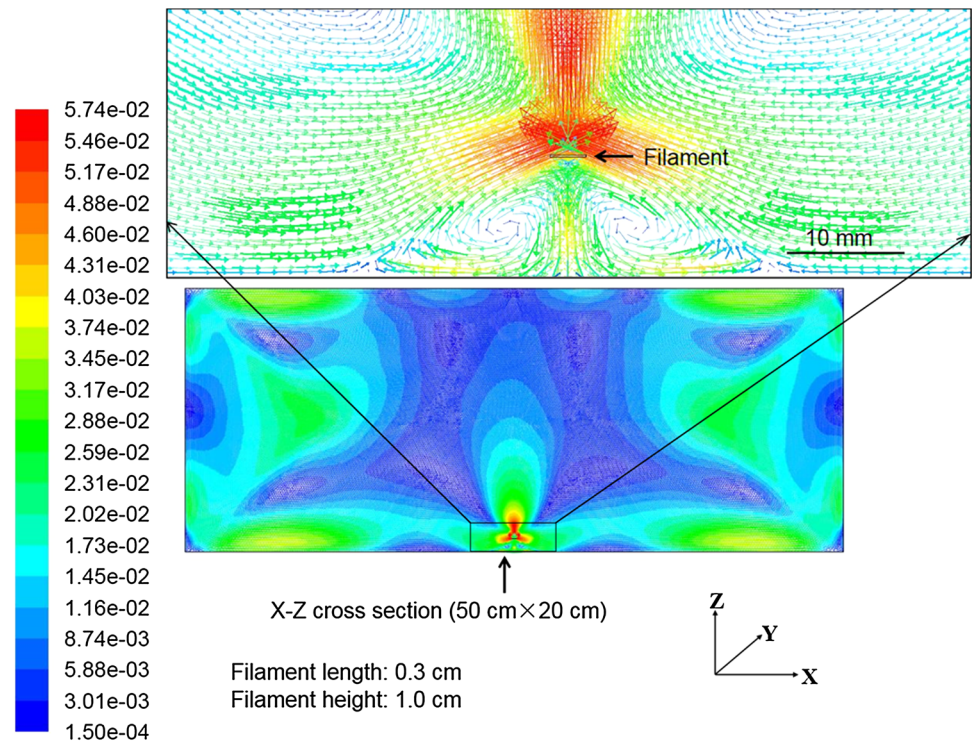


**Fig. 13** Two-dimensional simulation results for airflow in the  $X$ - $Z$  cross section (the bottom  $X$ - $Y$  section ( $Z = 0$ ) was the cold plate) containing 0.3-cm-long laser filament for an energy of 0.75 mJ with 1-cm filament height to the cold plate using the lens with 30-cm focal length. The velocity vectors are colored based on their velocity magnitude (m/s)



airflow above the filaments was not observed by side Mie scattering for shorter laser filaments (Figs. 3c-f, 7a-e), which is different from the simulation results (Figs. 11, 12, 13). This probably results from the weaker side Mie scattering because smaller-sized particles are produced in the

zone above the filament. Because the refrigerating unit is installed immediately below the bottom base plate, the temperature below the filament is much lower than that above the filament, and this results in a smaller temperature gradient in the zone from the laser filament to the top

plate. Consequently, much greater heat release is required to induce a stable updraft and vortices above the filament as compared to the vortices formation below the filament. Besides, the condensation nuclei above the filament are more difficult to grow into larger-sized particles owing to the higher temperature and low humidity there if the velocity of the laser-induced airflow is too low. There is a larger volume of air above the filament in the cloud chamber. A longer filament with the same intensity would heat a longer volume of air, and thus, a larger volume of air around the filament would also be driven to flow. In the simulation results of Figs. 10, 11, 12, 13, it is found that the airflow with higher velocities above the filaments (red and green zone above the filaments) occupies the zones with smaller areas in the cases of shorter filaments as compared to the airflow formed with the longest filament, indicating that intense and longer filaments could drive a larger area of air above the filament to flow. From this point of view, an intense and long filament is beneficial to promote the formation of updraft and large vortices above the filament. On the other hand, intense and shorter filaments can induce the formation of stable and well-contacted vortices below the filaments when the length of the filaments is comparable to twice the length of the vortex. Once stable and well-contacted vortices are generated below the filaments by the intense and shorter filaments, the growth of the condensation nuclei into large-sized particles would be speed up at the junction of two vortices and inside the vortices where the temperature is much lower and the humidity super-saturated (~230 %) [19, 24]. Thus, the airflow below the filaments induced by intense and shorter filaments was easily observed in the experiments owing to the stronger Mie scattering. Meantime, a stable thermal convection zone is also produced below the filaments due to the formation of strong vortices, and so the refrigerating bottom plate would bring away the heat release from the filaments via the continuous heat exchange with the rotating vortices. As a result, the larger temperature gradient in the zone from the laser filament to the bottom plate could be maintained, which drives the layer of mist initially formed close to the cold bottom flow into the inside of the vortices below the filaments where the pressure is lower. Thus, the bottom mist might be suppressed to move upward to some extent so that the airflow above the filaments is not easily observed.

The mass of the snow pile is strongly related to the formation of the stable vortices and airflow velocity. The collision efficiency would be enhanced if two vortices well contacted. Thus, the center junction of two vortices and inside of the vortices where the humidity is sub-saturated or super-saturated would accelerate growth of the condensation nuclei into large-sized particles through coalescence with small ice crystals or condensation of water vapor [19, 24]. In addition, the higher airflow velocity would increase the transport efficiency of water molecules carried by airflow involved

the vortices or passes by the snow pile. Therefore, much more snow would be produced by intense and short filaments for which the stable and well-contacted vortices with higher airflow velocities below the filaments commonly form.

## 6 Conclusions

We investigated femtosecond laser (800 nm/25 fs/1 kHz)-induced airflow patterns and snow formation under filaments of different lengths in a laboratory cloud chamber. The filaments with different lengths were generated by adjusting the incident laser energy when the lens focal length was fixed at 50 or 30 cm. The side signal intensity of the laser filaments, the airflow patterns, and the shapes and masses of the snow piles were compared. Both the airflow pattern and the mass of the snow pile are found to be closely related to the intensity and length of the filament. Intense and long laser filaments are beneficial in generating the updraft with vortices above the filament, while intense and short filaments tend to promote the formation of well-contacted vortices below the filament. The snow piles generated by different patterned airflows show oval shapes. We simulated the airflow in the cloud chamber numerically by assuming that the laser filament acts as a heat source. It was found the gap between the two vortices below the filaments changes as the filament length changes. The mechanisms of airflow and snow formation induced by different filaments were discussed. Considering the important role that airflow plays in the process of laser-assisted water condensation [17–19, 23, 24], this study will provide a reference for the filament selection in laser-induced water condensation applications.

**Acknowledgments** This work was supported by the National Basic Research Program of China (2011CB808100), the National Natural Science Foundation of China (11425418, 61475167, 11404354, 11174305 and 61221064), Shanghai Science and Technology Talent Project (No. 12XD1405200), and the State Key Laboratory Program of the Chinese Ministry of Science and Technology. Tiejun Wang also acknowledges the support from 100 Talent Program of Chinese Academy of Science and Shanghai Pujiang Program. See Leang Chin acknowledges the support of the Canada Research Chairs, the Natural Science and Engineering Research Council, and the Quebec Fund for Nature and Technology Research.

## References

1. P.B. Corkum, C. Rolland, T. Srinivasan-Rao, *Phys. Rev. Lett.* **57**, 2268 (1986)
2. J. Kasparian, R. Sauerbrey, S.L. Chin, *Appl. Phys. B* **71**, 877 (2000)
3. S.L. Chin, S.A. Hosseini, W. Liu, Q. Luo, F. Théberge, N. Aközbeke, A. Becker, V.P. Kandidov, O.G. Kosareva, H. Schroeder, *Can. J. Phys.* **83**, 863 (2005)
4. A. Couairon, A. Mysyrowicz, *Phys. Rep.* **441**, 47 (2007)

5. L. Bergé, S. Skupin, R. Nuter, J. Kasparian, J.-P. Wolf, *Rep. Prog. Phys.* **70**, 1633 (2007)
6. G. Méjean, J. Kasparian, J. Yu, E. Salmon, S. Frey, J.-P. Wolf, S. Skupin, A. Vinçotte, R. Nuter, S. Champeaux, L. Bergé, *Phys. Rev. E* **72**, 026611 (2005)
7. S. Champeaux, L. Bergé, D. Gordon, A. Ting, J. Peñano, P. Sprangle, *Phys. Rev. E* **77**, 036406 (2008)
8. J. Kasparian, M. Rodriguez, G. Méjean, J. Yu, E. Salmon, H. Wille, R. Bourayou, S. Frey, Y.-B. André, A. Mysyrowicz, R. Sauerbrey, J.-P. Wolf, L. Wöste, *Science* **301**, 61 (2003)
9. S.L. Chin, H.L. Xu, Q. Luo, F. Théberge, W. Liu, J.F. Daigle, Y. Kamali, P.T. Simard, J. Bernhardt, S.A. Hosseini, M. Sharifi, G. Méjean, A. Azarm, C. Marceau, O. Kosareva, V.P. Kandidov, N. Aközbek, A. Becker, G. Roy, P. Mathieu, J.R. Simard, M. Châteauneuf, J. Dubois, *Appl. Phys. B* **95**, 1 (2009)
10. P. Rairoux, H. Schillinger, S. Niedermeier, M. Rodriguez, F. Ronneberger, R. Sauerbrey, B. Stein, D. Waite, C. Wedekind, H. Wille, L. Wöste, C. Ziener, *Appl. Phys. B* **71**, 573 (2000)
11. X.M. Zhao, J.-C. Diels, C.Y. Wang, J.M. Elizondo, *IEEE J. Quantum Electron.* **31**, 599 (1995)
12. Y. Petit, S. Henin, J. Kasparian, J.-P. Wolf, *Appl. Phys. Lett.* **97**, 021108 (2010)
13. J. Kasparian, L. Wöste, J.-P. Wolf, *Opt. Photon. News* **21**, 22 (2010)
14. P. Rohwetter, J. Kasparian, K. Stelmaszczyk, Z. Hao, S. Henin, N. Lascoux, W.M. Nakaema, Y. Petit, M. Queißer, R. Salamé, E. Salmon, L. Wöste, J.-P. Wolf, *Nat. Photon.* **4**, 451 (2010)
15. S. Hennin, Y. Petit, P. Rohwetter, K. Stelmaszczyk, Z.Q. Hao, W.M. Nakaema, A. Vogel, T. Pohl, F. Schneider, J. Kasparian, K. Weber, L. Wöste, J.-P. Wolf, *Nat. Commun.* **2**, 456 (2011)
16. Y. Petit, S. Henin, J. Kasparian, J.-P. Wolf, P. Rohwetter, K. Stelmaszczyk, Z.Q. Hao, W.M. Nakaema, L. Wöste, A. Vogel, T. Pohl, K. Weber, *Appl. Phys. Lett.* **98**, 041105 (2011)
17. J. Ju, J. Liu, C. Wang, H. Sun, W. Wang, X. Ge, C. Li, S.L. Chin, R. Li, Z. Xu, *Opt. Lett.* **37**, 1214 (2012)
18. H. Sun, J. Liu, C. Wang, W. Wang, J. Ju, Z. Wang, X. Ge, C. Li, S.L. Chin, R. Li, Z. Xu, *Opt. Express* **21**, 9255 (2013)
19. J. Ju, H. Sun, A. Sridharan, T.-J. Wang, C. Wang, J. Liu, R. Li, Z. Xu, S.L. Chin, *Phys. Rev. E* **88**, 062803 (2013)
20. W. Liu, S. Petit, A. Becker, N. Aközbek, C.M. Bowden, S.L. Chin, *Opt. Commun.* **202**, 189 (2002)
21. H. Saathoff, S. Henin, K. Stelmaszczyk, M. Petrarca, R. Delagrèze, Z. Hao, J. Lüder, O. Möhler, Y. Petit, P. Rohwetter, M. Schnaiter, J. Kasparian, T. Leisner, J.-P. Wolf, L. Wöste, *Atmos. Chem. Phys.* **13**, 4593 (2013)
22. [http://en.wikipedia.org/wiki/Cloud\\_condensation\\_nuclei](http://en.wikipedia.org/wiki/Cloud_condensation_nuclei)
23. J. Ju, J. Liu, C. Wang, H. Sun, W. Wang, X. Ge, C. Li, S.L. Chin, R. Li, Z. Xu, *Appl. Phys. B* **110**, 375 (2013)
24. J. Ju, T. Leisner, H. Sun, A. Sridharan, T.-J. Wang, J. Wang, C. Wang, J. Liu, R. Li, Z. Xu, S.L. Chin, *Appl. Phys. B* **117**, 1001 (2014)
25. A. Talebpour, S. Petit, S.L. Chin, *Opt. Commun.* **171**, 285 (1999)
26. A. Talebpour, M. Abdel-Fattah, A.D. Bandrauk, S.L. Chin, *Laser Phys.* **11**, 68 (2001)
27. F. Théberge, W. Liu, P.T. Simard, A. Becker, S.L. Chin, *Phys. Rev. E* **74**, 036406 (2006)
28. Y.P. Deng, J.B. Zhu, Z.G. Ji, J.S. Liu, B. Shuai, R.X. Li, Z.Z. Xu, F. Théberge, S.L. Chin, *Opt. Lett.* **31**, 546 (2006)
29. Y.-H. Cheng, J.K. Wahlstrand, N. Jhajj, H.M. Milchberg, *Opt. Express* **21**, 4740 (2013)
30. B. Charfi, M.A. Harith, *Spectrosc. Acta Pt. B Atom. Spectr.* **57**, 1141 (2002)
31. A. Sarani, A.Yu. Nikiforov, C. Leys, *Phys. Plasmas* **17**, 063504 (2010)
32. J.K. Wahlstrand, N. Jhajj, E.W. Rosenthal, S. Zahedpour, H.M. Milchberg, *Opt. Lett.* **39**, 1290 (2014)
33. O. Lahav, L. Levi, I. Orr, R.A. Nemirovsky, J. Nemirovsky, I. Kaminer, M. Segev, O. Cohen, *Phys. Rev. A* **90**, 021801(R) (2014)
34. S.-B. Wen, X. Mao, C. Liu, R. Greif, R. Russo, *J. Phys. Conf. Ser.* **59**, 343 (2007)
35. G. Point, C. Milián, A. Couairon, A. Mysyrowicz, A. Houard, *J. Phys. B* **48**, 094009 (2015)
36. J. Papeer, M. Botton, D. Gordon, P. Sprangle, A. Zigler, Z. Henis, *New J. Phys.* **16**, 123046 (2014)
37. H. Sobral, M. Villagrán-Muniz, R. Navarro-González, A.C. Raga, *Appl. Phys. Lett.* **77**, 3158 (2000)
38. T. Taha, Z.F. Cui, *J. Membr. Sci.* **210**, 13 (2002)
39. F. Stratmann, A. Kiselev, S. Wurzler, M. Wendisch, J. Heintzenberg, R.J. Charlson, K. Diehl, H. Wex, S. Schmidt, *J. Atmos. Ocean. Technol.* **21**, 876 (2004)
40. F. Stratmann, M. Wilck, V. Žďimal, J. Smolík, *J. Phys. Chem. B* **105**, 11641 (2001)
41. W. Tao, *Numerical Heat Transfer*, Chap. 1 (Jiaotong University, Xi'an, 2001)
42. Q. Chen, *Build. Environ.* **31**, 233 (1996)
43. S.A. Hosseini, Q. Luo, B. Ferland, W. Liu, S.L. Chin, O.G. Kosareva, N.A. Panov, N. Aközbek, V.P. Kandidov, *Phys. Rev. A* **70**, 033802 (2004)
44. Q. Luo, A.A. Hosseini, W. Liu, J.-F. Gravel, O.G. Kosareva, N.A. Panov, N. Aközbek, V.P. Kandidov, G. Roy, S.L. Chin, *Appl. Phys. B* **80**, 35 (2005)